Doornbos, E., van den Ijssel, J., Lühr, H., Förster, M., Koppenwallner, G. (2010): Neutral density and crosswind determination from arbitrarily oriented multi-axis accelerometers on satellites. - Journal of Spacecraft and Rockets, 47, 4, 580-589

DOI: 10.2514/1.48114

# Neutral density and crosswind determination from arbitrarily oriented multi-axis accelerometers on satellites

Eelco Doornbos*and Jose van den IJssel*

*Delft University of Technology, 2629 HS Delft, The Netherlands*

Hermann Lühr†and Matthias Förster‡

*Helmholtz Centre Potsdam, GFZ - German Centre for Geosciences, 14473 Potsdam, Germany*

Georg Koppenwallner§

*Hypersonic Technology Göttingen, 37191 Katlenburg-Lindau, Germany*

**An iterative algorithm for determining density and crosswind from multi-axis accelerometer measurements on satellites is presented, which works independently of the orientation of the instrument in space. The performance of the algorithm is compared with previously published algorithms using simulated data for the CHAMP satellite. Without external error sources, the algorithm reduces RMS density errors from 0.7% to 0.03% and RMS wind errors from 38 m/s to 1 m/s in this test. However, the effect of errors in the instrument calibration and external models that are used in the density and wind retrieval are dominant for CHAMP. These lead to mostly systematic density errors of the order of ∼10–15%. The accuracy of the wind results when using the new algorithm is almost fully determined by the sensitivity of the cross-track acceleration component to calibration and radiation pressure modeling errors. The applicability of the iterative algorithm and the accuracy of its results is demonstrated by presenting CHAMP data from a period where the satellite was commanded to fly sideways, and comparing the density and wind results with those from**

*Researcher, Faculty of Aerospace Engineering, Department of Earth Observation and Space Systems
†Working Group Leader, Professor, Department 2.3: Earth's Magnetic Field
‡Scientist, Department 2.3: Earth's Magnetic Field
§Head, Professor, Senior Member AIAA

**adjacent days where the satellite was in its nominal attitude mode. These investigations result in recommendations for the design of future satellite accelerometer missions for thermosphere research.**

## Nomenclature

| | |
|---|---|
| $\alpha_{\mathrm{E}}$ | Energy flux accommodation coefficient, dimensionless |
| $\boldsymbol{a}$ | Acceleration, m/s$^2$ |
| $A$ | Area, m$^2$ |
| $\boldsymbol{C}$ | Normalized force coefficient, dimensionless |
| $c$ | Atmospheric constituent mass concentration, dimensionless |
| $\boldsymbol{d}$ | Acceleration direction residual, dimensionless |
| $m$ | Mass, kg |
| $\hat{\boldsymbol{n}}$ | Panel unit normal vector, dimensionless |
| $R$ | Rotation matrix from the inertial to the spacecraft body-fixed (SBF) frame, dimensionless |
| $r$ | Residual, percentage of the signal or m/s |
| $S$ | Calibration scale factor matrix (3×3 diagonal), dimensionless |
| $T$ | Atmospheric temperature, K |
| $T_{\mathrm{wall}}$ | Satellite wall temperature, K |
| $\hat{\boldsymbol{u}}_{\mathrm{up}}$ | Unit vector in the local vertical direction, dimensionless. |
| $\boldsymbol{v}$ | Velocity, m/s |
| $\boldsymbol{\omega}_{\oplus}$ | Angular velocity of the Earth's rotation with respect to inertial space, $\boldsymbol{\omega}_{\oplus} = (0, 0, 0.7292115 \cdot 10^{-4})^T$ rad/s.[1] |
| $\rho$ | Density, kg/m$^3$ |

*Subscripts*

| | |
|---|---|
| a | Aerodynamic force |
| alb | Earth albedo radiation pressure |
| bias | Calibration bias |
| c | Atmospheric corotation component of relative velocity |
| cal | Calibrated accelerometer measurement |
| D | Drag |
| i | Inertial |
| $i$ | Iteration index |
| IR | Earth infrared radiation pressure |
| $j$ | Atmospheric constituent index |
| $k$ | Panel index |

| | |
|---|---|
| L | Lift and sideways aerodynamic force |
| mod | Modeled aerodynamic |
| o | Orbital velocity component of relative velocity |
| obs | Observed aerodynamic |
| r | of the atmosphere relative to the satellite |
| $\rho$ | of density |
| $\mathrm{r}, 0$ | Initial value, ignoring the wind or modeling the in-track wind component |
| $\mathrm{r}, i$ | Solution after iteration $i$, including an accelerometer-derived wind component |
| raw | Raw, uncalibrated accelerometer data |
| srp | Solar radiation pressure |
| up | Vector component in the local vertical direction |
| $v$ | of wind speed |
| w | Wind with respect to an Earth-fixed atmosphere |
| x | Vector component in the $\mathrm{X_{SBF}}$ direction |
| y | Vector component in the $\mathrm{Y_{SBF}}$ direction |
| z | Vector component in the $\mathrm{Z_{SBF}}$ direction |

*Conventions*

| | |
|---|---|
| $\boldsymbol{a}$ | Vector |
| $a = \|\|\boldsymbol{a}\|\|$ | Vector magnitude |
| $\hat{\boldsymbol{a}} = \boldsymbol{a}/\|\|\boldsymbol{a}\|\|$ | Unit vector |
| $\boldsymbol{a}'$ | Vector for which the component projected on the local vertical direction is set to zero. |

# I. Introduction

Accelerometers carried by low-Earth orbiters such as CHAMP, GRACE, GOCE and the future Swarm satellites, provide important data for improving our understanding of thermospheric density and winds. The CHAMP and GRACE missions were not designed for studies of the thermosphere; they carry accelerometers in order to allow for the removal of non-gravitational signals from measured orbit perturbations due to inhomogeneities in the Earth's gravity field. Nevertheless, their application to thermosphere studies has resulted in density and wind data sets containing information at unprecedented levels of detail and coverage.

Analyses of accelerometer-derived density data sets resulted in the publication of a large number of scientific papers, on topics including the response to drivers such as solar EUV variability,[2,3] geomagnetic storms,[4–6] Joule heating,[7] solar flares,[8] solar wind streams;[9] and on phenomena such as the equatorial mass density anomaly,[10,11] upwelling in the cusp region,[12,13] travelling atmospheric disturbances[14] and solar terminator waves.[15,16] These inves-

tigations made use of density data processed using algorithms published by Bruinsma,[17,18] Sutton[5,19] and Lühr[10,13] and their coauthors.

Investigations of wind results from the CHAMP mission have started to appear in recent years as well. These papers can be classified by their focus on either the equatorial to mid-latitudes[15,20–23] or the polar regions.[24,25] An important early paper on wind derivation from accelerometer data is that by Marcos and Forbes[26] who analyzed triaxial accelerometer measurements from the SETA instrument flown on several spacecraft in the early 1980s. Recent publications on the derivation of winds from CHAMP data are provided by Liu[20] and Sutton[19] and their respective coauthors.

The current paper contributes to this research topic by presenting an improved, more generally applicable iterative density and wind derivation algorithm. The basic problem to be solved by such an algorithm is that the accelerometer delivers at most three orthogonal acceleration observations. However, there are at least four unknowns: Density and three orthogonal wind velocity components. The solution to this problem lies in the fact that the orbital velocity of the satellite is much greater than the wind velocity. The error in the total relative velocity, and therefore in the density, can be kept limited by assuming that the in-track wind speed is zero, or by applying an in-track wind value from an empirical model. Eliminating this unknown from the equation enables the determination of reasonably accurate density values, as well as wind speed components orthogonal to the in-track direction.

Section II describes the relative velocity components in more detail and discusses the relationship between models and observations of the aerodynamic acceleration. In Section III, the previously published algorithms are reviewed, after which the new algorithm is presented. Section IV provides an evaluation of the algorithm, and Section VI summarizes the main conclusions and recommendations from this work.

## II. Accelerations and velocities

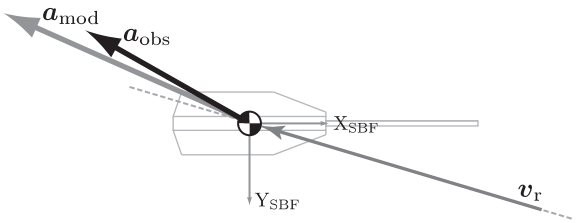


**Figure 1. Relative velocity, modeled and observed accelerations in the CHAMP spacecraft body-fixed (SBF) XY plane. CHAMP is viewed from the top.**

Figure 1 provides a simple schematic view of the three vectors of importance for a density and wind retrieval algorithm: The observed and modeled aerodynamic accelerations $\boldsymbol{a}_{\mathrm{obs}}$ and

$\boldsymbol{a}_{\mathrm{mod}}$ are shown originating in the centre of mass of the satellite. In addition, the relative velocity $\boldsymbol{v}_{\mathrm{r}}$ of the atmosphere with respect to the spacecraft is shown. This quantity is partly observed and partly modeled, as will be explained below. Note that due to the asymmetrical shape of the satellite with respect to the flow, the acceleration is in general not exactly aligned with the relative velocity, as indicated by the dashed guide line.

Due mainly to the approximate character of the modeled density and wind speed, the modeled and observed aerodynamic acceleration vectors initially do not match in magnitude and direction. It is the purpose of the new algorithm to find those density and wind values, which when replacing the original values make these accelerations match.

Before more detailed descriptions of the previous and new algorithms are provided, the relationship between the parameters in Figure 1 and the way in which they can be obtained from satellite observation data sets and models will be described. The description in the following Sections will refer to the instruments and data products of the current generation of accelerometer missions (CHAMP and GRACE) and to the external models (atmospheric models, force models, etc.) that are currently available. The new algorithm is not limited by the use of these data sets and models however. It can be just as well applied to equivalent data from historical or future accelerometer missions and using future improvements to external models.

### II.A. Relative velocity

The relative velocity of the atmosphere with respect to the spacecraft is the sum of contributions from the inertial velocity of the spacecraft in its orbit $\boldsymbol{v}_{\mathrm{o}}$, the velocity caused by the corotating atmosphere $\boldsymbol{v}_{\mathrm{c}}$, and the velocity of winds $\boldsymbol{v}_{\mathrm{w}}$, with respect to an Earth-fixed atmosphere.

$$\boldsymbol{v}_{\mathrm{r}} = \boldsymbol{v}_{\mathrm{o}} + \boldsymbol{v}_{\mathrm{c}} + \boldsymbol{v}_{\mathrm{w}} = -R\boldsymbol{v}_{\mathrm{i}} + R(\boldsymbol{\omega}_{\oplus} \times \boldsymbol{r}_{\mathrm{i}}) + \boldsymbol{v}_{\mathrm{w}} \tag{1}$$

The rotation matrix $R$ from the inertial to the satellite body-fixed (SBF) frame is obtained from star camera observations; the inertial satellite position and velocity, $\boldsymbol{r}_{\mathrm{i}}$ and $\boldsymbol{v}_{\mathrm{i}}$, are obtained by precise orbit determination using tracking observations from the satellite's GPS receiver; $\boldsymbol{\omega}_{\oplus}$ is the Earth's angular velocity vector. These first two contributors to $\boldsymbol{v}_{\mathrm{r}}$ are known at a much higher accuracy than the wind velocity $\boldsymbol{v}_{\mathrm{w}}$. If model values for $\boldsymbol{v}_{\mathrm{w}}$ are required, these can be obtained from the horizontal wind model HWM07[27] for example, and subsequently transformed to the SBF frame.

This paper will use the notation $\boldsymbol{v}_{\mathrm{r},0}$ or $\boldsymbol{v}_{\mathrm{r},i=0}$ to indicate an initial guess of the relative velocity, by either neglecting winds or using a wind model. The notation $\boldsymbol{v}_{\mathrm{r},i}$ will designate a relative velocity which already includes an accelerometer-derived wind component.

### II.B. Observed aerodynamic acceleration

The observed aerodynamic acceleration $\boldsymbol{a}_{\text{obs}}$ is obtained from the raw accelerometer data after calibration and removal of non-aerodynamic acceleration signals.

Calibration is performed by multiplying the raw acceleration vector with a 3×3 diagonal scale factor matrix, and adding a bias vector:

$$\boldsymbol{a}_{\text{cal}} = S\boldsymbol{a}_{\text{raw}} + \boldsymbol{a}_{\text{bias}} \tag{2}$$

The scale factors can often be considered (nearly) constant,[28] while the bias is known to vary on timescales of days and more, under the influence of ageing effects and temperature variations. Changes to the satellite software or switches between the redundant on-board electronics parts can cause abrupt changes in the calibration parameters. The determination of the calibration parameters used in this study for the in-track accelerometer observations is described by Van Helleputte,[29] who made use of GPS observations. This method was found to be not sufficiently accurate for the cross-track accelerometer observations, for which an alternative method was applied, as discussed at the end of Section IV.A.

Various non-aerodynamic signals should be removed from the accelerometer data, including accelerations due to activity of cold gas thrusters for attitude control. If a set of two opposing thrusters are not perfectly balanced, as is often the case, they introduce a residual signal in the linear acceleration, besides the intended angular acceleration. Data around the activation times of these thrusters should therefore be removed. A less obvious example of accelerations that should be removed from the data are those due to mechanical forces caused by electrical current changes on the satellite.[30]

Finally, modeled accelerations due to radiation pressure from the Sun $\boldsymbol{a}_{\text{srp}}$, Earth albedo $\boldsymbol{a}_{\text{alb}}$ and Earth infrared radiation $\boldsymbol{a}_{\text{IR}}$ are computed and removed from the calibrated and edited accelerometer data $\boldsymbol{a}_{\text{cal}}$, to arrive at the observed aerodynamic acceleration vector $\boldsymbol{a}_{\text{obs}}$.

$$\boldsymbol{a}_{\text{obs}} = \boldsymbol{a}_{\text{cal}} - \boldsymbol{a}_{\text{srp}} - \boldsymbol{a}_{\text{alb}} - \boldsymbol{a}_{\text{IR}} \tag{3}$$

The modeling of these radiation pressure forces comprises several non-trivial components: Modeling of eclipse and semi-shadow conditions for solar radiation pressure,[31–33] values for the reflectivity and infrared emissivity of Earth surface elements,[32,34] and models of the geometry and optical properties of the satellite surfaces. Simple panelized models (of limited accuracy) are available in literature for CHAMP[17] and GRACE.[35] These provide areas $A_k$ and unit normal vectors $\hat{\boldsymbol{n}}_k$ for 8 to 15 panels for CHAMP and GRACE. But these models do not provide information on the shape and relative position of each panel. More accurate

geometry models, with an arbitrary number of precisely positioned and shaped panels, can be created in specialized software, such as ANGARA,[32] based on CAD drawings of the satellites.

The modeled radiation pressure accelerations can then be calculated by evaluating either analytical equations,[17,19] or applying a Monte Carlo Test Particle method[32] on the panelized representation of the satellite. The advantage of the latter approach is that the contributions of multiple reflections of photons and shadowing of parts of the satellite by other parts are automatically taken into account.

### II.C. Modeled aerodynamic acceleration

The modeled aerodynamic acceleration vector $\boldsymbol{a}_{\mathrm{mod}}$ is a function of a large number of parameters. Since the aerodynamic acceleration is found to be proportional to the density $\rho$, and the square of the relative velocity $v_{\mathrm{r}}^2$, it is expressed in vector form as:

$$\boldsymbol{a}_{\mathrm{mod}} = \boldsymbol{C}_{\mathrm{a}} \frac{A_{\mathrm{ref}}}{m} \frac{1}{2} \rho v_{\mathrm{r}}^2 \tag{4}$$

If the aerodynamic force components perpendicular to the velocity direction (lift and sideways forces) are omitted, the aerodynamic acceleration reduces to just a drag acceleration, which is by definition in the direction of the velocity relative to the spacecraft. Eq. (4) then reduces to an equation containing the scalar drag coefficient $C_{\mathrm{D}}$ instead of the force coefficient vector $\boldsymbol{C}_{\mathrm{a}}$:

$$\boldsymbol{a}_{\mathrm{D}} = C_{\mathrm{D}} \frac{A_{\mathrm{ref}}}{m} \frac{1}{2} \rho v_{\mathrm{r}}^2 \hat{\boldsymbol{v}}_{\mathrm{r}} \tag{5}$$

Ignoring the much smaller lift and sideways force components, both perpendicular to drag, is standard practice in applications such as orbit determination,[36] but it introduces errors in the density and wind derivation from accelerometer data. Therefore we will continue here by using the more general vector eq. (4).

The aerodynamic force coefficient vector $\boldsymbol{C}_{\mathrm{a}}$ is a function of the satellite shape, its orientation with respect to the flow and of the nature of the aerodynamic interaction with the atmospheric particles. These aspects will be discussed further below. The area $A_{\mathrm{ref}}$ is a fixed reference value, used to make $\boldsymbol{C}_{\mathrm{a}}$ dimensionless. The mass $m$ is obtained by subtracting from the satellite launch mass the amount of cold gas used, which is logged in the satellite's housekeeping data.

The computation of $\boldsymbol{C}_{\mathrm{a}}$ is for a large part analogous to the computation of radiation pressure accelerations, referred to above. Similar computational techniques can be used, including an evaluation of analytical expressions of the forces acting on a panelized rep-

resentation of the satellite outer surfaces,[17,19,37] or applying a Monte Carlo Test Particle computation.[32]

The description of the interaction of atmospheric particles with each surface element can be split into two distinct contributions: That of the incident particle flux, and that of the reflected or reemitted particle flux. Both contribute to the drag, however lift and sideways aerodynamic forces are mainly generated by the reflected particle flux.

An exact description of the acceleration contribution by the incident particle flux is possible, but it requires knowledge on the magnitude and direction of the relative velocity, $\boldsymbol{v}_\mathrm{r}$, with respect to the surface element, the atmospheric temperature $T$, and the relative concentrations $c_j$, of the different particles species ($j = \mathrm{O}_2, \mathrm{N}_2, \mathrm{O}, \mathrm{He}, \mathrm{H}, \ldots$) having different molecular masses $m_j$. These latter parameters determine the velocity of the random motion of the molecules and atoms, which is to be superimposed on the bulk velocity $\boldsymbol{v}_\mathrm{r}$ of the atmosphere with respect to the satellite surface.

Earlier analyses of CHAMP and GRACE data[5,17–19] used aerodynamic expressions by Cook[38] simplified for compact satellite shapes, which ignored the influence of the random thermal motion of the atoms and molecules on the aerodynamic force.[39] This resulted in lower drag coefficients and higher densities with larger fluctuations for CHAMP and GRACE. Sutton recently made an update of his aerodynamic model,[40] which showed a much improved fidelity of his density data,[41] a difference which we have been able to confirm in our own processing.

Contrary to previous analyses,[17] we do not use a mean molecular mass, but calculate $\boldsymbol{C}_\mathrm{a}$ as the concentration-weighted sum of contributions from the various constituents $j$, since the dependence of these contributions on the molecular mass is highly non-linear. When a small concentration of light-weight constituents (such as Helium) is present, this does not affect the mean molecular mass by much. However, these light-weight particles, because of their high thermal velocity, will have a higher collision rate with the satellite's side panels, that are oriented nearly parallel to the stream, than the heavier constituents (such as oxygen or nitrogen). This will result in significantly larger values of $\boldsymbol{C}_\mathrm{a}$, especially for the elongated satellite shapes of the current accelerometer missions.

A description of the reflected particle flux requires a model of the gas-surface interaction, which specifies the angular distribution and energy flux of the reflected particles. Unfortunately, experimental data on gas-surface interaction[42,43] is limited to only a subset of the range of conditions under which current space accelerometers are making measurements. This puts an exact physical representation of this contribution to the aerodynamic force out of reach.

Ideally, information on the gas-surface interaction, as well as in-situ observations of aerodynamic model parameters like the temperature $T$ and concentrations $c_j$, should be measured

by independent instruments on the accelerometer-carrying satellite. Since the current and planned accelerometer missions lack the required instrumentation, we have to rely on empirical atmosphere models such as NRLMSISE-00,[44] simplified gas-surface interaction models, and some educated guesses.

Such simplified gas-surface interaction models contain parameters like the energy flux accommodation coefficient $\alpha$,[45] which determines whether the particles retain their mean kinetic energy (for $\alpha = 0$) or acquire the temperature of the spacecraft surface $T_{\text{wall}}$ (for $\alpha = 1$). Another possible parameter is the Maxwell coefficient $\sigma$, which determines the fraction of particles that leaves the surface in either a completely diffuse ($\sigma = 1$) or completely specular ($\sigma = 0$) angular distribution.

With these caveats in mind, the rarefied aerodynamic equations for flat panels, derived by Sentman[46] are currently seen as an appropriate choice for use in the processing of CHAMP and GRACE data. Sentman's equations take into account the random thermal motion of the incident particles, and assume a completely diffuse distribution of the reflected particle flux. This is reasonably consistent with the limited data from in-orbit gas-surface interaction experiments,[42,47] which suggests that over the altitude range of CHAMP and GRACE, the angular distribution is likely within a few percent of complete diffuse reemission ($\sigma \gtrsim 0.95$), and that the energy flux accommodation is quite high ($\alpha \gtrsim 0.8$). Moe[45] introduced the energy flux accommodation coefficient $\alpha$ as a parameter in Sentman's equations. Our implementation of this modification of Sentman's equations for accelerometer data processing is similar to the one recently published by Sutton,[40] therefore we shall not repeat the equations here.

For the purposes of this paper, it is sufficient to keep in mind that $\boldsymbol{C}_{\text{a}}$ is an intricate function of the relative velocity and parameters related to the spacecraft and surrounding atmosphere:

$$\boldsymbol{C}_{\text{a}} = \boldsymbol{C}_{\text{a}}(\boldsymbol{v}_{\text{r}}, c_j, T, A_k, \hat{\boldsymbol{n}}_k, T_{\text{wall,k}}, \alpha, \dots) \tag{6}$$

# III. Processing algorithms

## III.A. Direct algorithms for CHAMP and GRACE

Previously published algorithms made use of assumptions about the orientation of the accelerometer in space. For CHAMP and GRACE, the accelerometer instruments are carefully mounted near the satellite centre of mass, with an orientation so that their three axes can be considered perfectly aligned with the spacecraft body-fixed (SBF) axes. The spacecraft are under active attitude control, which keeps these axes within a few degrees of the orbit-fixed

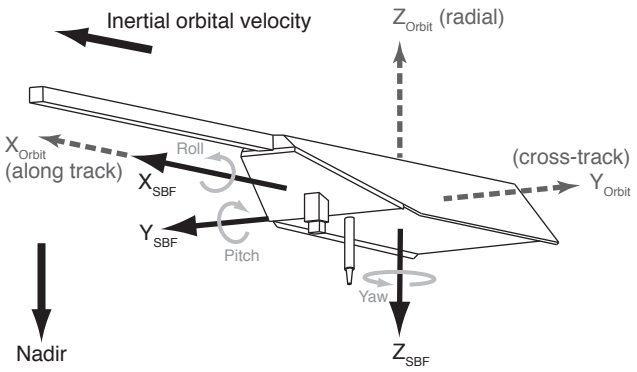


**Figure 2. Definition of spacecraft body-fixed (SBF) axes for CHAMP and their relative orientation with respect to the orbit-fixed axes in the satellite's nominal attitude.**

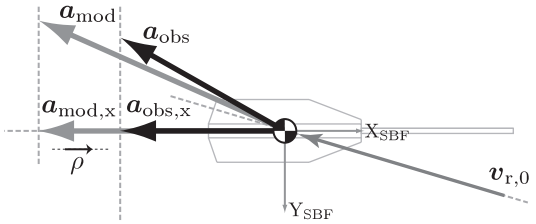


**Figure 3. Schematic representation of the direct determination of density from the projection of accelerations on the $X_{SBF}$ axis.**

along-track, cross-track and radial directions (see Figure 2). The relative orientation of these axes can be expressed in roll, pitch and yaw Euler angles.

Because these Euler angles are relatively small, the inertial orbital velocity of the satellite is kept closely aligned with the $X_{SBF}$ axis. It is known from orbital mechanics that accelerations in the velocity direction are the most effective in changing the orbital energy, and therefore have a much larger effect on the orbit than accelerations of similar magnitude in perpendicular directions. This means that the $X_{SBF}$ axis of the accelerometer can be more accurately calibrated using positioning data from the GPS instrument[29] than the $Y_{SBF}$ and $Z_{SBF}$ axes, even without taking into account the larger measured signal. This consideration leads to an approach for density determination[17–19] where only the projection of the aerodynamic acceleration on the $X_{SBF}$ axis is used, as shown schematically in Figure 3. The density can be solved directly from the X-component of the vector equation (4):

$$\rho = \frac{2m}{A_{\mathrm{ref}} v_{\mathrm{r},0}^2} \frac{a_{\mathrm{obs,x}}}{C_{\mathrm{a,x}}} \tag{7}$$

Information from the acceleration component in the $Y_{SBF}$ direction, closely aligned with the cross-track direction, can be used to derive data on the wind speed in that direction. Sutton[19] describes two approaches. In the first approach, $\boldsymbol{C}_{\mathrm{a}}$ in eq. (4) is expanded using analytical equations, evaluated by summation over a 13-panel satellite model, which incor-

porates the computation of both drag and lift on each 2D panel. The resulting equation is quadratic with respect to $v_{w,y}$, which can then be solved, resulting in an expression depending on $a_{obs,y}$ and $\rho$. Sutton names this approach the single axis method, even though information from both the X- and Y-axes is required, if $\rho$ is to be substituted from eq. (7).

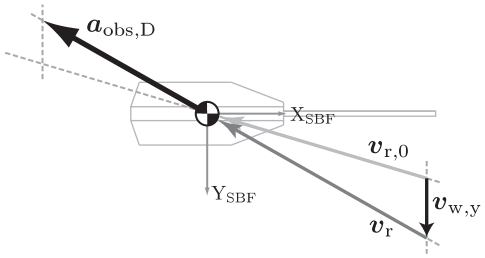


**Figure 4. Schematic representation of the direct determination of wind from the accelerometer $Y_{SBF}$ axis.**

The second approach is named the dual-axis method by Sutton,[19] and can be found in an earlier paper by Liu[20] as well. The method requires that the lift and sideways forces are negligible, or are modeled and removed from the acceleration beforehand, so that only the observed acceleration due to drag $\boldsymbol{a}_{obs,D}$ remains. The authors do not specify exactly how the lift and sideways forces should be modeled, but we have adopted the following approach: First, a new modeled aerodynamic acceleration is computed according to eq. (4), now with the density from eq. (7) and with the a-priori relative velocity $\boldsymbol{v}_{r,0}$ as inputs. This acceleration vector $\boldsymbol{a}_{mod}$ can then be decomposed into a drag component, by projection on the relative velocity direction, and a perpendicular lift plus sideways force component, by subtraction of that drag component from the original modelled acceleration. In equations:

$$\boldsymbol{a}_{mod,D} = (\boldsymbol{a}_{mod} \cdot \hat{\boldsymbol{v}}_{r,0})\hat{\boldsymbol{v}}_{r,0}, \quad \boldsymbol{a}_{mod,L} = \boldsymbol{a}_{mod} - \boldsymbol{a}_{mod,D} \tag{8}$$

The modeled lift plus sideways aerodynamic force $\boldsymbol{a}_{mod,L}$ is then subtracted from the observed aerodynamic acceleration, to arrive at the observed drag.

$$\boldsymbol{a}_{obs,D} = \boldsymbol{a}_{obs} - \boldsymbol{a}_{mod,L} \tag{9}$$

The velocity and drag acceleration are by definition in the same direction, so that the wind can be determined from a simple geometrical consideration (see Figure 4). Expressed in the form of an equation, $\rho$ and $\boldsymbol{C}_D$ disappear when the Y-component of eq. (5) is divided by the X-component, and $v_{w,y}$ is solved for after substitution of eq. (1), resulting in:

$$v_{w,y} = \frac{a_{obs,D,y}}{a_{obs,D,x}} v_{r,0,x} - v_{r,0,y} \tag{10}$$

A similar wind determination could in principle be performed for the $Z_{SBF}$ axis. However, the aerodynamic acceleration in this direction is in general too small compared to errors in the instrument calibration, radiation pressure model and lift force model. In addition, on the CHAMP accelerometer, this $Z_{SBF}$ component suffers from a malfunction which prevents the acquisition of accurate data.[48]

### III.B. Discussion of the direct algorithms

The schematic representations in Figures 3 and 4 clearly show that when the angle between the relative velocity and the $X_{SBF}$ axis gets larger, the errors in the density and wind increases. For the extreme case where this angle approaches 90 degrees, density values will approach zero, while the wind speed will go to infinity. Of course, the angles in these figures are exaggerated for clarity, in the case of CHAMP and GRACE under nominal attitude control. The roll, pitch and yaw Euler angles are kept within $\pm 1$ degree for GRACE and $\pm 2$ degrees for CHAMP. For the future Swarm mission, the attitude will likely be somewhat more loosely controlled, probably to within $\pm 4$ degrees.

These attitude angles only determine the alignment of the body-fixed frame with the inertial velocity vector. The contributions to the relative velocity vector by the co-rotation of the atmosphere and thermosphere winds can be equally important. The atmospheric co-rotation velocity over the equator depends on the altitude, ranging from 483–502 m/s at 250–500 km. This increases the maximum angle between the relative velocity and the $X_{SBF}$ axis by 3.6–3.8 degrees. The wind speed, which under most conditions is within the range of about 0–200 m/s, can reach peak velocities in the polar regions of up to 500–1000 m/s,[24,25] causing the incidence angle to reach peak values of 8–10 degrees. In principle, the accuracy of the derived density and wind speed should be independent of these angles.

Another limiting factor of the direct algorithm results from the dependence of $\boldsymbol{C}_\mathrm{a}$ on $\boldsymbol{v}_\mathrm{r}$. The methods use an initial value $\boldsymbol{v}_{\mathrm{r},0}$, composed of the orbit and co-rotation velocity, and neglect or model the in-track wind velocity. After the derivation of the cross-track wind $v_{\mathrm{w,y}}$ however, there is a better estimate of the relative velocity:

$$\boldsymbol{v}_{\mathrm{r},i=1} = \boldsymbol{v}_{\mathrm{r},0} + \boldsymbol{v}_{\mathrm{w,y}} \tag{11}$$

where the index $i$ is an iteration counter. This new relative velocity leads to a new value of $\boldsymbol{C}_\mathrm{a}$ (according to eq. 6) and therefore to a new value of $\rho$. The change in $\boldsymbol{C}_\mathrm{a}$ also leads to a change in the lift and sideways components of the aerodynamic acceleration, which are to be removed from $\boldsymbol{a}_\mathrm{obs}$ to arrive at $\boldsymbol{a}_\mathrm{obs,D}$, yielding a new value for $v_{\mathrm{w,y}}$. This chain of dependencies indicates that an iterative algorithm is more suitable to determine the density and wind speed with high accuracy.

## III.C. Iterative algorithm

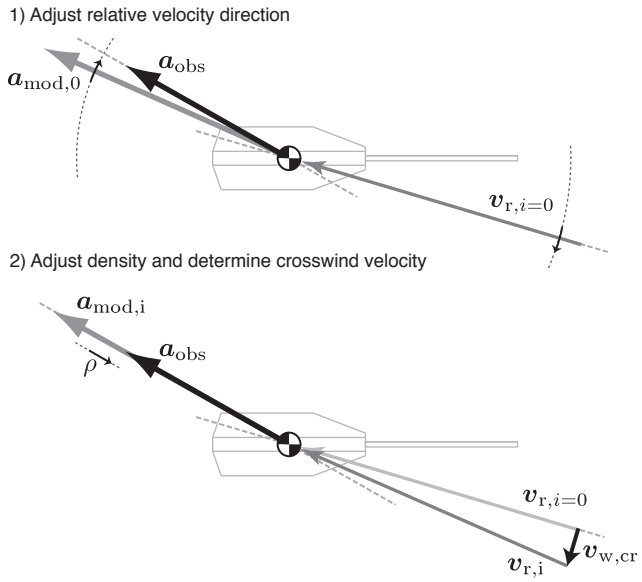


**Figure 5. Schematic representation of the iterative wind and density derivation.**

This section presents an iterative algorithm, which avoids the restrictions and sources of error discussed in the previous section. Figure 5 illustrates schematically the principle of the algorithm in two steps. The goal of the algorithm is to make the modeled aerodynamic acceleration $\boldsymbol{a}_{\mathrm{mod}}$ match the direction (top panel) and subsequently the magnitude (bottom panel) of the aerodynamic acceleration observed by the accelerometer $\boldsymbol{a}_{\mathrm{obs}}$. This is achieved by first modifying the direction of the relative velocity vector $\boldsymbol{v}_{\mathrm{r}}$, without modifying its magnitude, until the modeled acceleration direction matches that of the observed acceleration. Subsequently the density $\rho$ is modified, so that the magnitude of the accelerations matches.

The adjustment to the orientation is made by a rotation of the relative velocity about the local vertical direction, indicated by the unit vector $\hat{\boldsymbol{u}}_{\mathrm{up}}$. The acceleration components projected on this direction will be set to zero. To simplify the notation, a prime is added to indicate this modification of the acceleration vectors, which is applied repeatedly:

$$\boldsymbol{a}' = \boldsymbol{a} - (\boldsymbol{a} \cdot \hat{\boldsymbol{u}}_{\mathrm{up}})\ \hat{\boldsymbol{u}}_{\mathrm{up}} \tag{12}$$

We will use the sum of the orbital and co-rotation velocities as our a-priori relative velocity for now:

$$\boldsymbol{v}_{\mathrm{r},i=0} = \boldsymbol{v}_{\mathrm{o}} + \boldsymbol{v}_{\mathrm{c}} \tag{13}$$

The possibility of including modeled in-track and vertical wind velocities in the algorithm computation will be discussed in Section III.D.

While modifying the direction of the velocity and modeled acceleration vectors, the magnitude of the acceleration is not of importance. We therefore make use of the unit vectors $\hat{\boldsymbol{a}}'_{\mathrm{obs}}$ and $\hat{\boldsymbol{a}}'_{\mathrm{mod}}$, and according to eq. (4) substitute $\hat{\boldsymbol{C}}_{\mathrm{a}}$ for the latter. We can now define our measure of the acceleration direction residual:

$$\boldsymbol{d} = \hat{\boldsymbol{a}}'_{\mathrm{obs}} - \hat{\boldsymbol{a}}'_{\mathrm{mod},i} = \hat{\boldsymbol{a}}'_{\mathrm{obs}} - \hat{\boldsymbol{C}}'_{\mathrm{a},i}(\boldsymbol{v}_{\mathbf{r},\boldsymbol{i}}, \dots) \tag{14}$$

In practice, if the magnitude of $\boldsymbol{d}$ is below a certain predefined threshold $\epsilon$, convergence has been reached. Otherwise, another iteration is required. The convergence criterium is thus:

$$d = ||\boldsymbol{d}|| < \epsilon \tag{15}$$

The unit vector representing the direction of the velocity adjustment for the current iteration is defined to be perpendicular to both the relative velocity and the rotation axis:

$$\hat{\boldsymbol{v}}_{\mathrm{adj},i} = \frac{\boldsymbol{v}_{\mathrm{r},i} \times \hat{\boldsymbol{u}}_{\mathrm{up}}}{||\boldsymbol{v}_{\mathrm{r},i} \times \hat{\boldsymbol{u}}_{\mathrm{up}}||} \tag{16}$$

Next, to start our numerical differentiation, two relative velocity vectors are formed, which keep the magnitude of the unadjusted relative velocity, but which are rotated slightly in both directions with respect to the relative velocity of the current iteration:

$$\boldsymbol{v}_{\mathrm{r}}^{+} = ||\boldsymbol{v}_{\mathrm{r},i}|| \frac{\boldsymbol{v}_{\mathrm{r},i} + \delta\hat{\boldsymbol{v}}_{\mathrm{adj},i}}{||\boldsymbol{v}_{\mathrm{r},i} + \delta\hat{\boldsymbol{v}}_{\mathrm{adj},i}||}, \quad \boldsymbol{v}_{\mathrm{r}}^{-} = ||\boldsymbol{v}_{\mathrm{r},i}|| \frac{\boldsymbol{v}_{\mathrm{r},i} - \delta\hat{\boldsymbol{v}}_{\mathrm{adj},i}}{||\boldsymbol{v}_{\mathrm{r},i} - \delta\hat{\boldsymbol{v}}_{\mathrm{adj},i}||} \tag{17}$$

These modified relative velocities will result in modified modelled acceleration directions, for which we apply the model of eq. (6). The result from both rotation directions is substituted into eq. (14):

$$\boldsymbol{d}^{+} = \hat{\boldsymbol{a}}_{\mathrm{obs}} - \hat{\boldsymbol{C}}'_{\mathrm{a}}(\boldsymbol{v}_{\mathrm{r}}^{+}, \dots), \quad \boldsymbol{d}^{-} = \hat{\boldsymbol{a}}_{\mathrm{obs}} - \hat{\boldsymbol{C}}'_{\mathrm{a}}(\boldsymbol{v}_{\mathrm{r}}^{-}, \dots) \tag{18}$$

The vector difference between the two velocity vectors is:

$$\Delta\boldsymbol{v}_{\mathrm{r}} = \boldsymbol{v}_{\mathrm{r}}^{+} - \boldsymbol{v}_{\mathrm{r}}^{-} \tag{19}$$

And the effect of this velocity rotation on the acceleration direction residual is:

$$\Delta d = ||\boldsymbol{d}^{+}|| - ||\boldsymbol{d}^{-}|| \tag{20}$$

Now, all the elements are in place to compute the next iteration of the relative velocity, which keeps the magnitude of the original velocity, but changes the direction.

$$\boldsymbol{v}_{\mathrm{r},i+1} = ||\boldsymbol{v}_{\mathrm{r},i}|| \frac{\boldsymbol{v}_{\mathrm{r},i} - d(\Delta \boldsymbol{v}_{\mathrm{r}}/\Delta d)}{||\boldsymbol{v}_{\mathrm{r},i} - d(\Delta \boldsymbol{v}_{\mathrm{r}}/\Delta d)||} \tag{21}$$

At this point eqs. (14) and (15) are reevaluated. If the convergence criterium of eq. (15) is met, we can proceed computing the crosswind speed and mass density.

$$\boldsymbol{v}_{\mathrm{w,cr}} = \boldsymbol{v}_{\mathrm{r},i} - \boldsymbol{v}_{\mathrm{r},i=0} \tag{22}$$

$$\rho = \frac{2m}{A_{\mathrm{ref}} v_{\mathrm{r},i}^2} \frac{||\boldsymbol{a}'_{\mathrm{obs}}||}{||\boldsymbol{C}'_{\mathrm{a},i}||} \tag{23}$$

### III.D. Modeling of in-track and vertical winds

In the description of the algorithms above, we have not discussed the possible effect on the aerodynamics of wind components other than the cross-track component. Since we are interested in retrieving the crosswind $\boldsymbol{v}_{\mathrm{w,cr}}$ from the accelerometer data, a model value for this component should not be included in the a-priori relative velocity of eq. (13). A model value for the in-track wind $\boldsymbol{v}_{\mathrm{w,it}}$, and the wind in the direction of the rotation axis $\boldsymbol{v}_{\mathrm{w,z}}$ could be applied in that equation however. These can be computed by projecting the full model wind on the unit vectors in these directions.

$$\boldsymbol{v}_{\mathrm{w,it}} = (\boldsymbol{v}_{\mathrm{w,mod}} \cdot \hat{\boldsymbol{v}}_{\mathrm{r}})\ \hat{\boldsymbol{v}}_{\mathrm{r}} \tag{24}$$

$$\boldsymbol{v}_{\mathrm{w,up}} = (\boldsymbol{v}_{\mathrm{w,mod}} \cdot \hat{\boldsymbol{u}}_{\mathrm{up}})\ \hat{\boldsymbol{u}}_{\mathrm{up}} \tag{25}$$

Since $\hat{\boldsymbol{v}}_{\mathrm{r}}$ changes its direction during the iterative process described in the previous Section, eq. (24) will have to be reevaluated and $\boldsymbol{v}_{\mathrm{r}}$ in eqs. (17) and (21) be updated after each iteration step.

## IV. Algorithm tests

### IV.A. Error assessment using simulated accelerometer data

The direct and iterative algorithms were tested using simulated aerodynamic acceleration data, in order to verify their correct implementation and to assess the accuracy of their results, both in the absence and presence of errors in the input data and models.

The simulated aerodynamic acceleration data were generated by applying eq. (4), using modeled density $\rho_{\mathrm{m}}$ and wind $\boldsymbol{v}_{\mathrm{w,m}}$ values from the NRLMSISE-00 density model[44] and

the HWM07 wind model.[27] The real CHAMP attitude and orbit data were used both in the generation of this simulated acceleration data and in the application of the retrieval algorithms. The accuracy of the algorithm results, comprising of the density $\rho$ and crosswind $v_{\mathrm{w,y}}$ or $v_{\mathrm{w,cr}}$ can then be tested by examining density and wind residuals $r_\rho$ and $r_v$.

The density residuals are expressed as percentages, relative to the simulated density signal:

$$r_\rho = \frac{\rho - \rho_{\mathrm{m}}}{\rho_{\mathrm{m}}} \cdot 100\% \tag{26}$$

The wind residuals are defined as the differences between the retrieved wind speed and the modeled wind speed's projection on the direction of the retrieved wind speed:

$$r_v = v_{\mathrm{w,y}} - \boldsymbol{v}_{\mathrm{w,m}} \cdot \hat{\boldsymbol{v}}_{\mathrm{w,y}} \quad \text{or} \quad r_v = v_{\mathrm{w,cr}} - \boldsymbol{v}_{\mathrm{w,m}} \cdot \hat{\boldsymbol{v}}_{\mathrm{w,cr}} \tag{27}$$

Six cases for simulated errors are defined. In the first case, labeled "Identical input", the exact same models and input data were used in the retrieval algorithm that had been originally applied in the creation of the simulated accelerations. This allows for an assessment of the errors that are purely inherent in the algorithm.

However, it is also important to evaluate the algorithms under the influence of the uncertainties in the input data and models. In two further cases, named "$\mathrm{X_{SBF}}$ offset" and "$\mathrm{Y_{SBF}}$ offset", a value of 10 nm/s$^2$ was added to the simulated acceleration data in either direction, before applying the algorithms. For each single measurement, such an offset could be the result of an error in the instrument calibration, or due to errors in the removal of radiation pressure and attitude thruster accelerations. Each of these error sources comes with its own temporal variation of the acceleration error, and their effects can either add up or (partly) cancel each other out. Therefore, the constant 10 nm/s$^2$ offset introduced here should be viewed as just a crude approximation, which should nevertheless give some idea of the sensitivity of the density and wind derivation algorithms. In the fourth test case, named "In-track wind", the HWM07 modeled wind in the in-track direction was neglected in the density and crosswind derivation algorithms.

Two further test cases are used to assess the effect of force model errors. The simulated aerodynamic accelerations were generated with a value of $\alpha = 0.93$ for the energy flux accommodation parameter in the aerodynamic model. In the "Energy accommodation" case, this value was changed to $\alpha = 0.88$ for the density and wind retrieval. This 5% difference can be used to represent one aspect of the inherent uncertainty in the gas-surface interaction modeling. The final test case, named "Panel model", is used to represent the uncertainty in the satellite geometry model for complexly shaped satellites such as CHAMP. Our own adjusted panellised geometrical model of the CHAMP satellite[49] used in the simulated data generation was replaced by an alternative one[17] in the density and wind retrieval. This

| *Direct algorithm* | min. | mean | max. | RMS | std. |
|---|---|---|---|---|---|
| Identical input | -3.3 | 0.0 | 5.5 | 0.7 | 0.7 |
| $X_{SBF}$ offset | -17.4 | -2.7 | 3.8 | 3.1 | 1.5 |
| $Y_{SBF}$ offset | -3.3 | 0.0 | 5.5 | 0.7 | 0.7 |
| In-track wind | -10.8 | 0.2 | 14.3 | 2.2 | 2.1 |
| Energy accomm. | -4.8 | -1.7 | 3.7 | 1.9 | 0.7 |
| Panel model | 3.5 | 7.8 | 14.0 | 7.9 | 0.9 |
| *Iterative algorithm* | min. | mean | max. | RMS | std. |
| Identical input | -0.5 | -0.0 | 0.0 | 0.0 | 0.0 |
| $X_{SBF}$ offset | -17.4 | -2.9 | 0.5 | 3.2 | 1.4 |
| $Y_{SBF}$ offset | -12.3 | -0.3 | 4.5 | 1.6 | 1.6 |
| In-track wind | -10.9 | 0.2 | 13.6 | 2.0 | 2.0 |
| Energy accomm. | -2.1 | -1.6 | -0.7 | 1.6 | 0.2 |
| Panel model | 5.7 | 8.1 | 9.0 | 8.1 | 0.3 |

**Table 1. Statistics of the density retrieval residuals, in percentages of the density signal.**

replacement amounts to a reduction in frontal area of around 14% when the satellite is viewed along the $X_{SBF}$ axis (front), and of 8% when viewed along the $Y_{SBF}$ axis (side).

The statistics of the density retrieval residuals over the complete year 2004 ($\sim$3.15 million measurements), are presented in Table 1. During this year, CHAMP flew only in its nominal attitude mode for which the direct algorithm is applicable. The data in the table shows that the iterative algorithm leads to lower density residuals than the direct approach in the "Identical input" case. With the 10 nm/s$^2$ $Y_{SBF}$ acceleration offset, this ranking is shifted however, because the iterative algorithm is sensitive to this acceleration component, while the direct algorithm is not. Both algorithms show an equal sensitivity to in-track wind errors. The direct algorithm seems slightly more sensitive to the force-model related errors, though, if judged by the standard deviations. Note that for the force model related errors, the mean values are generally larger than the standard deviations, indicating that these accelerometer-derived density data are affected by mostly systematic errors. The data will therefore be more suitable to studies of relative changes in density than for use in modeling approaches which require absolute density values.

In the wind residual statistics, presented in Table 2, the advantage of the iterative algorithm over the direct approach is evident, certainly for the "Identical input" case. For both algorithms, the 10 nm/s$^2$ error introduced in the $Y_{SBF}$ direction of the accelerations has a very large detrimental effect on the accuracy of the crosswind speed, leading to maximum errors of 915 m/s (iterative) and 1283 m/s (direct). Such very large wind errors will occur in the real data processing when the aerodynamic acceleration signal in the $Y_{SBF}$ direction

| *Direct* | min. | mean | max. | RMS | std. |
|---|---|---|---|---|---|
| Identical input | -225 | -1 | 202 | 38 | 38 |
| $X_{SBF}$ offset | -226 | -2 | 210 | 44 | 44 |
| $Y_{SBF}$ offset | -173 | 209 | 1285 | 236 | 110 |
| In-track wind | -228 | -2 | 205 | 38 | 38 |
| Energy accomm. | -258 | -1 | 222 | 52 | 52 |
| Panel model | -262 | -2 | 224 | 54 | 54 |
| *Iterative* | min. | mean | max. | RMS | std. |
| Identical input | -9 | -0 | 10 | 1 | 1 |
| $X_{SBF}$ offset | -44 | 3 | 81 | 12 | 12 |
| $Y_{SBF}$ offset | -242 | 81 | 915 | 140 | 114 |
| In-track wind | -9 | -0 | 10 | 1 | 1 |
| Energy accomm. | -55 | -0 | 51 | 21 | 21 |
| Panel model | -52 | 0 | 49 | 22 | 22 |

**Table 2. Statistics of the wind retrieval residuals, in m/s.**

is small compared to the instrument calibration, instrument noise and radiation pressure errors for that direction. These large wind errors are therefore prevalent at conditions of low density, such as at higher orbital altitudes and lower solar activity levels. For this reason, it is not currently possible to acquire an accurate crosswind derivation from the GRACE satellites, which are at a higher altitude than CHAMP. A related important factor in this respect is the magnitude of cross-track radiation pressure accelerations and related acceleration errors. These occur when the satellite's orbital plane is near-perpendicular to the Sun-Earth vector (dawn-dusk orbit). We have also encountered particularly extreme wind errors around eclipse transitions. A small discrepancy between the modeled and true eclipse geometry will lead to short periods with an incorrect application or removal of the full modeled radiation pressure acceleration, which has a maximum magnitude of around 40 $nm/s^2$ for CHAMP, leading to wind errors far exceeding 1000 m/s.

The results in Table 2 show that the crosswind derivation is practically insensitive to errors in the along-track wind. The other error sources also have only minor effects in comparison to the $Y_{SBF}$ offset.

It should be clear that a large aerodynamic signal strength, a careful calibration of the accelerometer in the crosswind direction and an accurate modeling of cross-track radiation pressure accelerations are a necessity for the derivation of accurate crosswind results.

The $Y_{SBF}$ (cross-track) calibration for the CHAMP and GRACE satellites using GPS data is problematic,[29] because of the relatively low acceleration signal, and because of the limited capability of accelerations in this direction to perturb the orbit, compared to along-

track accelerations. Both limitations are the result of fundamental orbital dynamics in combination with the tight attitude control of the spacecraft, as discussed at the start of Section III.A. We therefore adopted an alternative approach to calibrate CHAMP's $Y_{SBF}$ accelerometer data, analogous to Sutton.[19] We took density observations derived using the direct method from the $X_{SBF}$ data, and combined these with the aerodynamic satellite model to arrive at simulated observations for the $Y_{SBF}$ data. The accelerometer data for this direction was then calibrated by estimating the biases that minimize the difference between the data and these simulated observations. We have checked the reliability of these biases by comparing the local time variation of the zonal wind from ascending arcs with those from descending arcs and found no systematic difference. An error in the $Y_{SBF}$ biases would influence the ascending and descending wind profiles in opposite directions.

Users of accelerometer-derived density and wind data should be aware of the level and nature of errors inherent in these data, as presented in this Section.

### IV.B. CHAMP accelerometer data for different satellite attitude modes

The CHAMP mission provides an interesting possibility for further assessment of the capabilities of the iterative algorithm. There have been two periods, on October 7 and 8, 2001, and on November 6, 2002, when CHAMP was commanded to fly sideways with respect to its nominal altitude for about 7 orbital revolutions (∼11 hours). Figure 6 shows the CHAMP calibrated accelerometer data with modelled radiation pressure accelerations removed, for three days surrounding the sideways-flying attitude period on November 6, 09:00–20:00 UTC. The shaded areas correspond to three orbits of data starting at 12:00 UTC each day, and lasting about 1.5 hours, which will be used in further analysis below. The three small drawings at the top of the Figure give an indication of the CHAMP satellite geometry as viewed from the nominal orbital velocity direction.

Notice that the drag acceleration is in the $Y_{SBF}$ direction during the sideways-flying period, and is approximately 3 times larger than the drag in the $X_{SBF}$ direction during the surrounding nominal (forward-flying) period. This higher drag acceleration in the sideways-flying period is the result of the larger frontal area, but this is offset to some extent by a lower drag coefficient.

Basically, these two attitude modes present us with two completely different aerodynamic shapes with respect to the flow. In the forward-flying configuration, CHAMP is a long and slender shape, with only a small frontal area, but with its large solar panel and bottom surfaces oriented parallel to the stream. A considerable fraction of the aerodynamic acceleration on the shape in this orientation is due to collisions with these parallel surfaces, which cause an increase in the drag coefficient. In the sideways-flying configuration, CHAMP is a wide and short object, with most of the aerodynamic force caused by near-frontal collisions, and

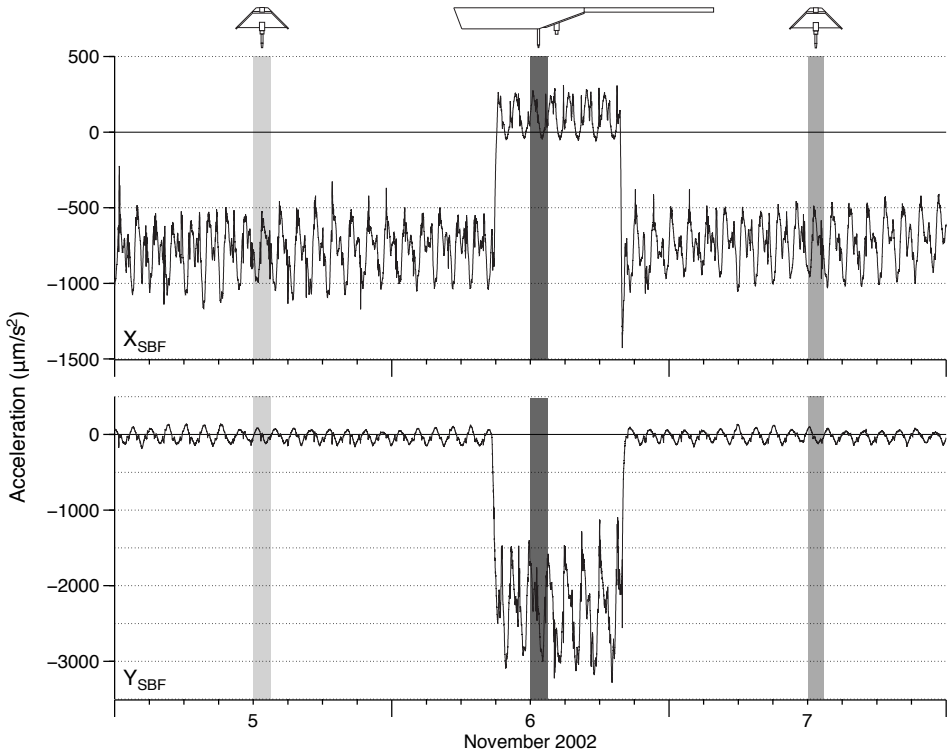


**Figure 6. Calibrated CHAMP accelerometer data with modeled radiation pressure removed, for three days surrounding the November 6, 2002 sideways-flying period.**

only a relatively small contribution by surfaces parallel to the stream.

Unfortunately, the satellite was not designed to operate in the sideways-flying mode for extended periods of time. Both the attitude control actuation and the thermal environment of the accelerometer instrument will have been quite different than during nominal operations on the surrounding days. The different orientation of the instrument also has consequences for the accuracy of the instrument calibration (see the discussion at the end of Section IV.A). These considerations are important to keep in mind in the interpretation of this data.

Figure 7 shows the density and wind retrieval results using the iterative algorithm for the three orbits indicated with background shading in Figure 6. The black, light gray and dark gray solid lines represent the accelerometer-derived density and wind results for the sideways-flying day and the nominal previous and next day, respectively. These shades also correspond to the model results for these orbits, plotted with open circles in the same figure.

The local solar time (LST) at the equator crossings for these orbits was approximately 09:40 (ascending) and 21:40 (descending) during this period. The shaded background indicates where the satellite was in eclipse. The 24-hour interval between the three orbits was chosen so that each of the orbits crosses the auroral zones at approximately the same magnetic local time, thus reducing variability by keeping the sampling characteristics as similar as possible. Since proxies of solar EUV radiation and geomagnetic activity also show

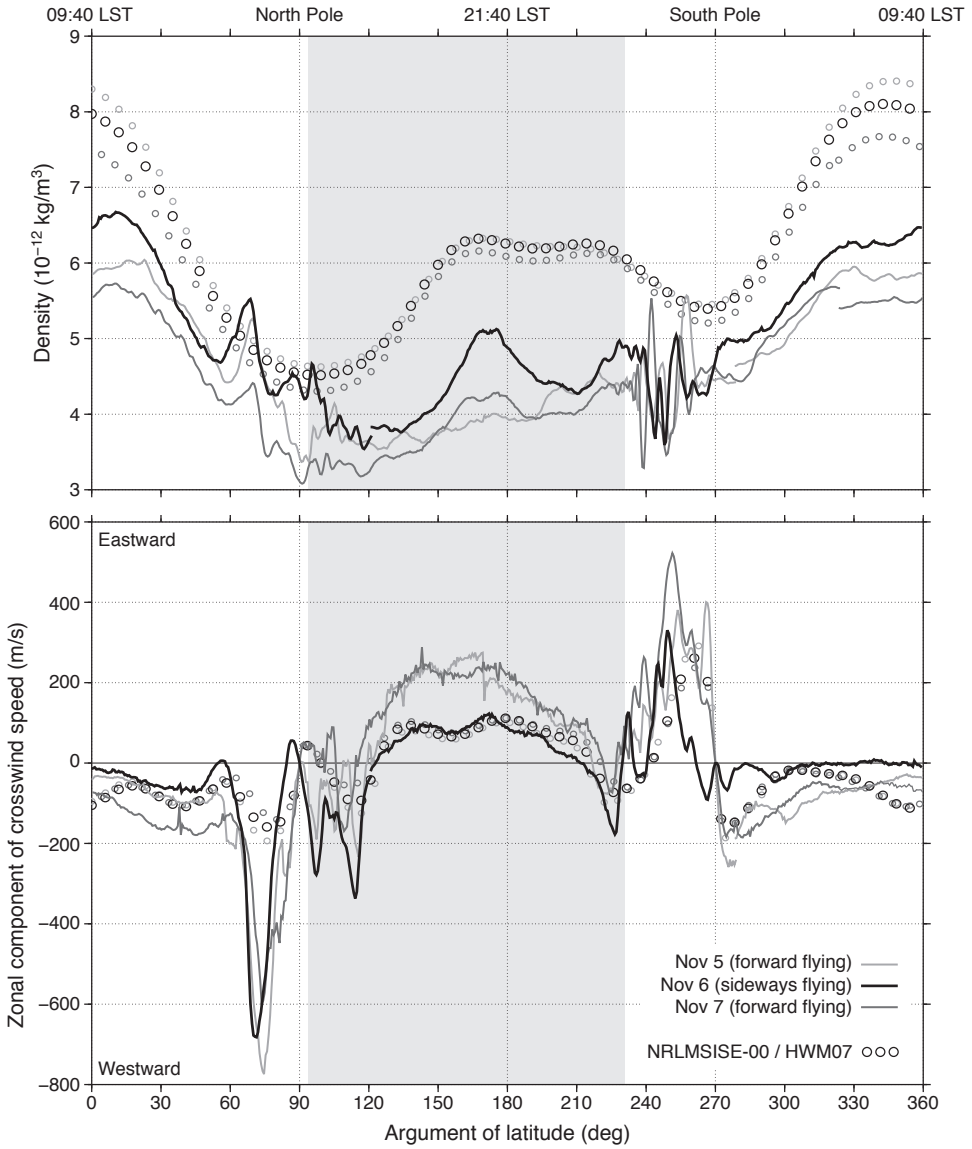


**Figure 7. Comparison of three orbits of CHAMP accelerometer-derived and modeled density and wind data from the November 6, 2002 sideways-flying period and two surrounding days of nominal attitude.**

little variation during this period, the NRLMSISE-00 and HWM07 model curves for the orbits on the three different days show largely the same magnitudes and patterns. The large scale patterns are determined by variations in orbital altitude, between 396/400 km at the evening/morning equator crossings and 417 km over the poles, and by thermospheric features such as the diurnal density bulge, causing the absolute maximum in density around the morning equator crossing.

The density retrieved by CHAMP resembles this behaviour, but is in general around 15–25% lower than the model values. It is unlikely that such a large offset can be fully attributed to systematic errors in the accelerometer-derived data alone, so it should be at least partly due to the density model error as well. Such offsets between model and observed

density values is seen in other data sets and at other times in our CHAMP data set as well, but a further analysis must be delegated to a future paper. Another significant difference between the density model data and CHAMP results are the sharp spikes at high latitudes, especially in the Southern Hemisphere evening sector, which could be related to upwelling in the polar cusp region,[12,13] and/or errors due to poorly modeled in-track wind variations.

The CHAMP density data from the sideways-flying period shows largely the same features as the data for the two surrounding days, but it is on average slightly higher. This difference could be due to different errors in the satellite geometry and aerodynamic interaction modeling for the two attitude modes, but it is not possible to distinguish such an effect from the natural density variability over these days.

We shall now turn our attention to the zonal wind data in Figure 7. The model zonal winds at low- and mid-latitudes are at around 100 m/s, eastward in the evening and westward in the morning, away from the sub-solar density bulge. The modeled winds at high latitudes show a complex behaviour with much shorter wavelengths, related to geomagnetic energy inputs, with peaks of around 300 m/s eastward in the Southern Hemisphere and of around 200 m/s westwards in the Northern Hemisphere. The most obvious feature in the CHAMP-derived data is this Northern Hemisphere peak, which reaches an amplitude of over 700 m/s, nearly three times the model prediction. These strong westward winds blowing from the day to the night side across the prenoon sector are common in the auroral region.[24,25] The smaller Southern Hemisphere peak shows a better consistency between the HWM07 model and CHAMP-derived data than this Northern Hemisphere peak.

At low- and mid-latitudes, the HWM07 model predictions for the three consecutive days overlap to a large extent. It is therefore interesting to see that the CHAMP-derived zonal winds from the two days with a nominal orientation also show a large degree of consistency with each other, even though the maximum amplitudes are significantly higher than the model values. The wind derived from the sideways-flying period is inconsistent in comparison with those from the surrounding days, but more consistent in comparison with the model results, especially on the descending (evening) pass.

There are several reasons to believe that the wind data from the sideways-flying period is the most accurate. First of all, the compact satellite shape is less sensitive to errors in the aerodynamic and geometrical modeling than the elongated shape of the nominal configuration. Secondly, the larger frontal area when flying sideways results in a larger drag signal. This makes the wind derivation less susceptible to acceleration errors due to issues with the calibration and solar radiation pressure modeling. The fact that the evening wind data seems less noisy than the equivalent data on the surrounding days supports this reasoning. And thirdly, and perhaps a bit more tentatively, since the accelerometer axes for the along-track and cross-track axes are switched during the manoeuvre, the wind

determination can benefit from the accurate GPS-derived calibration of the $X_{SBF}$ axis, during the surrounding days. This axis is in the crucial crosswind direction during the sideways-flying period.

The difference between the low latitude crosswind data on the sideways-flying days and the surrounding days amounts to 50–150 m/s. If we assume that the sideways-flying crosswind data is accurate, and that the day-to-day natural variability of the low-latitude zonal wind is limited, this means that the wind errors in the nominal configuration are at this level as well. This conclusion is in line with the results of Table 2.

Data from the other sideways-flying period in October 2001 leads to similar conclusions. This data is not presented here because the density and wind results are less clear than those for the 2002 event. This is mainly due to atypically large instrument calibration errors and the larger day-to-day density variability at that time.

Further studies into the instrument calibration and geometrical and aerodynamic modeling are required to reconcile the wind data from both attitude modes.

## V. Recommendations for future missions

It should be noted once more that the current generation of accelerometer-carrying satellite missions (CHAMP, GRACE, GOCE and Swarm) were not designed for thermosphere density and wind studies as part of their primary mission objectives. The experience gained in the study of the CHAMP data in particular, and the development and analysis of the iterative algorithm presented in this paper, has lead to several recommendations for the development of possible future thermosphere missions, with the aim to reduce density and wind errors.

First of all, a compact and simple design of the satellite external shape, without protruding antennae, camera baffles, booms, etc., will reduce the uncertainty in geometrical and aerodynamic satellite modeling, which will result in a more reliable estimate of absolute density values. The availability of additional instruments on accelerometer missions, which could make contemporaneous in-situ measurements of the atmospheric temperature, molecular mass, in-track wind, and other parameters important for gas-surface interaction, would increase the accuracy of the aerodynamic calculations required for the accelerometer processing, as discussed in Section II.C. At the same time, such instruments would provide valuable data for atmospheric and aerodynamic modeling in general, which could in turn aid in a more accurate reprocessing of historical accelerometer datasets.

A large area-to-mass ratio of the satellite will increase the acceleration signal, which is especially beneficial for wind derivation. Flying at high solar activity and low altitude will help in that respect as well, but that is of course limiting to a mission's sampling

characteristics. A high eccentricity orbit might aid in calibration and the separate fine-tuning of radiation pressure and aerodynamic satellite models, but again at the cost of the beneficial atmospheric sampling characteristics of circular orbits.

Finally, the example of CHAMP's sideways-flying data shows that a more versatile or more loosely defined attitude control of an irregularly shaped satellite will provide data that can be used to identify and possibly reduce density and crosswind errors. If the attitude control can be designed such that each of the three accelerometer axes can spend a sufficient amount of time, in turn, in the satellite flight direction, this could be beneficial for the instrument calibration using orbit tracking data, and reduce the crosswind error in particular. The data processing of such a mission is possible using the iterative algorithm presented here.

## VI. Conclusions

In contrast to the previously published direct algorithms for deriving density and wind from accelerometer data, the iterative algorithm introduced in this paper can be applied in situations without a close alignment of the accelerometer axes with the along-track and cross-track directions. In fact, it can be used for arbitrary orientations of the accelerometer axes in space. An analysis using simulated CHAMP data shows that errors due to assumptions on the orientation are significantly reduced when the new algorithm is applied. However, this analysis also shows that errors in the instrument calibration and input models that are common in the use of both algorithm types lead to more significant density and wind errors than the errors in the algorithms. Users of the current CHAMP and GRACE data (and possibly GOCE and Swarm data in the future as well), should be aware of the level and nature of errors inherent in these data. The investigation of these algorithms and their related error sources has led to recommendations for improvements of possible future dedicated accelerometer-carrying space missions for studies of the thermosphere.

## VII. Acknowledgements

This work was started as part of a study[49] funded by the European Space Agency's General Studies Program. The authors wish to thank Michael Kern, Roger Haagmans, Bent Fritsche, Nelli Eswein, David Rees, Tom van Helleputte and Pieter Visser for their contributions during the course of this project. Work at GFZ (M. Förster) was supported by the Deutsche Forschungsgemeinschaft (DFG).

# References


[1]Groten, E., "Report of special commission 3 of IAG - fundamental constants," *XXII IAG General Assembly*, 1999.

[2]Guo, J., Wan, W., Forbes, J. M., Sutton, E., Nerem, R. S., Woods, T., Bruinsma, S., and Liu, L., "Effects of solar variability on thermosphere density from CHAMP accelerometer data," *Journal of Geophysical Research*, Vol. 112, No. A10308, 2007.

[3]Müller, S., Lühr, H., and Rentz, S., "Solar and magnetospheric forcing of the low latitude thermospheric mass density as observed by CHAMP," *Annales Geophysicae*, Vol. 27, No. 5, 2009, pp. 2087–2099.

[4]Liu, H. and Lühr, H., "Strong disturbances of the upper thermospheric density due to magnetic storms: CHAMP observations," *Journal of Geophysical Research*, Vol. 110, No. A09829, 2005.

[5]Sutton, E., Forbes, J., and Nerem, R., "Global thermospheric neutral density and wind response to the severe 2003 geomagnetic storms from CHAMP accelerometer data," *Journal of Geophysical Research*, Vol. 110, No. A09S40, 2005.

[6]Burke, W., Lin, C., Hagan, M., Huang, C., Weimer, D., Wise, J., Gentile, L., and Marcos, F., "Storm time global thermosphere: A driven-dissipative thermodynamic system," *Journal of Geophysical Research*, Vol. 114, No. A06306, 2009.

[7]Sutton, E., Forbes, J., and Knipp, D., "Rapid response of the thermosphere to variations in Joule heating," *Journal of Geophysical Research*, Vol. 114, No. A04319, 2009.

[8]Liu, H., Lühr, H., Watanabe, S., Köhler, W., and Manoj, C., "Contrasting behavior of the thermosphere and ionosphere in response to the 28 October 2003 solar flare," *Journal of Geophysical Research*, Vol. 112, No. A077305, 2007.

[9]Lei, J., Thayer, J. P., Forbes, J. M., Sutton, E. K., Nerem, R. S., Temmer, M., and Veronig, A. M., "Global thermospheric density variations caused by high-speed solar wind streams during the declining phase of solar cycle 23," *Journal of Geophysical Research*, Vol. 113, No. A11303, 2008.

[10]Liu, H., Lühr, H., Henize, V., and Köhler, W., "Global distribution of the thermospheric total mass density derived from CHAMP," *Journal of Geophysical Research*, Vol. 110, No. A04301, 2005.

[11]Liu, H., Lühr, H., and Watanabe, S., "Climatology of the equatorial thermospheric mass density anomaly," *Journal of Geophysical Research*, Vol. 112, No. A05305, 2007.

[12]Lühr, H., Rother, M., Köhler, W., Ritter, P., and Grunwaldt, L., "Thermospheric upwelling in the cusp region: Evidence from CHAMP observations," *Geophysical Research Letters*, Vol. 31, No. 6, 2004.

[13]Rentz, S. and Lühr, H., "Climatology of the cusp-related thermospheric mass density anomaly, as derived from CHAMP observations," *Annales Geophysicae*, Vol. 26, No. 9, 2008, pp. 2807–2823.

[14]Bruinsma, S. L. and Forbes, J. M., "Properties of traveling atmospheric disturbances (TADs) inferred from CHAMP accelerometer observations," *Advances in Space Research*, Vol. 43, No. 3, 2009, pp. 369–376.

[15]Liu, H., Lühr, H., and Watanabe, S., "A solar terminator wave in thermospheric wind and density simultaneously observed by CHAMP," *Geophysical Research Letters*, Vol. 36, No. L10109, 2009.

[16]Miyoshi, Y., Fujiwara, H., Forbes, J. M., and Bruinsma, S. L., "Solar terminator wave and its relation to the atmospheric tide," *Journal of Geophysical Research*, Vol. 114, No. A07303, 2009.

[17]Bruinsma, S. and Biancale, R., "Total densities derived from accelerometer data," *Journal of Spacecraft and Rockets*, Vol. 40, No. 2, 2003, pp. 230–236.

[18]Bruinsma, S., Tamagnan, D., and Biancale, R., "Atmospheric densities derived from CHAMP/STAR accelerometer observations," *Planetary and Space Science*, Vol. 52, No. 4, 2004, pp. 297–312.

[19]Sutton, E. K., Nerem, R. S., and Forbes, J. M., "Density and winds in the thermosphere deduced from accelerometer data," *Journal of Spacecraft and Rockets*, Vol. 44, No. 6, 2007, pp. 1210–1219.

[20]Liu, H., Lühr, H., Watanabe, S., Köhler, W., Henize, V., and Visser, P., "Zonal winds in the equatorial upper thermosphere: Decomposing the solar flux, geomagnetic activity, and seasonal dependencies," *Journal of Geophysical Research*, Vol. 111, No. A07307, 2006.

[21]Häusler, K., Lühr, H., Rentz, S., and Köhler, W., "A statistical analysis of longitudinal dependencies of upper thermospheric zonal winds at dip equator latitudes derived from CHAMP," *Journal of Atmospheric and Solar-Terrestrial Physics*, Vol. 69, No. 12, 2007, pp. 1419–1430.

[22]Lühr, H., Häusler, K., and Stolle, C., "Longitudinal variation of F region electron density and thermospheric zonal wind caused by atmospheric tides," *Geophysical Research Letters*, Vol. 34, No. L16102, 2007.

[23]Häusler, K. and Lühr, H., "Nonmigrating tidal signals in the upper thermospheric zonal wind at equatorial latitudes as observed by CHAMP," *Annales Geophysicae*, Vol. 27, No. 6, 2009, pp. 2643–2652.

[24]Lühr, H., Rentz, S., Ritter, P., Liu, H., and Häusler, K., "Average thermospheric wind pattern over the polar regions, as observed by CHAMP," *Annales Geophysicae*, Vol. 25, No. 5, 2007, pp. 1093–1101.

[25]Förster, M., Rentz, S., Köhler, W., Liu, H., and Haaland, S. E., "IMF dependence of high-latitude thermospheric wind pattern derived from CHAMP cross-track measurements," *Annales Geophysicae*, Vol. 26, No. 6, 2008, pp. 1581–1595.

[26]Marcos, F. and Forbes, J., "Thermospheric winds from the satellite electrostatic triaxial accelerometer system," *Journal of Geophysical Research*, Vol. 90, 1985, pp. 6543–6552.

[27]Drob, D., Emmert, J., Crowley, G., Picone, J., Shepherd, G., Skinner, W., Hays, P., Niciejewski, R., Larsen, M., She, C., Meriwether, J., Hernandez, G., Jarvis, M., Sipler, D., Tepley, C., O'Brien, M., Bowman, J., Wu, Q., Murayama, Y., Kawamura, S., Reid, I., and Vincent, R., "An empirical model of the Earth's horizontal wind fields: HWM07," *Journal of Geophysical Research*, Vol. 113, No. A12304, 2008.

[28]Tapley, B. D., Ries, J. C., Bettadpur, S., and Cheng, M., "Neutral density measurements from the Gravity Recovery and Climate Experiment Accelerometers," *Journal of Spacecraft and Rockets*, Vol. 6, No. 44, 2007, pp. 1220–1225.

[29]Van Helleputte, T., Doornbos, E., and Visser, P., "CHAMP and GRACE accelerometer calibration by GPS-based orbit determination," *Advances in Space Research*, Vol. 43, No. 12, 2009, pp. 1890–1896.

[30]Flury, J., Bettadpur, S., and Tapley, B. D., "Precise accelerometry onboard the GRACE gravity field satellite mission," *Advances in Space Research*, Vol. 42, No. 8, 2008, pp. 1414–1423.

[31]Vokrouhlický, D., Farinella, P., and Mignard, F., "Solar radiation pressure perturbations for Earth satellites, I. A complete theory including penumbra transitions," *Astronomy and Astrophysics*, Vol. 280, 1993, pp. 295–312.

[32]Fritsche, B., Ivanov, M., Kashkovsky, A., Koppenwallner, G., Kudryavtsev, A., Voskoboinikov, U., and Zhukova, G., "Radiation pressure forces on complex spacecraft, Final report, ESOC contract 11908/96/D/IM," Tech. rep., HTG, Germany and ITAM, Russia, 1998.

[33]Adhya, S., Sibthorpe, A., Ziebart, M., and Cross, P., "Oblate Earth eclipse state algorithm for low-Earth orbiting satellites," *Journal of Spacecraft and Rockets*, Vol. 41, No. 1, 2004, pp. 157–159.

[34]Knocke, P. C., *Earth radiation pressure effects on satellites*, Ph.D. thesis, Center for Space Research, The University of Texas at Austin, 1989.

[35]Bettadpur, S., "Gravity Recovery and Climate Experiment Product Specification Document (Rev

4.5 – February 20, 2007)," Tech. Rep. GRACE 327-720/CSR-GR-03-02, Center for Space Research, The University of Texas at Austin, 2007.

[36]Montenbruck, O. and Gill, E., *Satellite orbits : models, methods and applications*, Springer-Verlag, 2000.

[37]Fuller, J. D. and Tolson, R. H., "Improved method for estimation of spacecraft free-molecular aerodynamic properties," *Journal of Spacecraft and Rockets*, Vol. 46, No. 5, 2009, pp. 938–948.

[38]Cook, G. E., "Satellite drag coefficients," *Planetary and Space Science*, Vol. 13, No. 10, 1965, pp. 929–946.

[39]Koppenwallner, G., "Comment on special section: New perspectives on the satellite drag environments of Earth, Mars and Venus," *Journal of Spacecraft and Rockets*, Vol. 45, No. 6, 2008, pp. 1324–1326.

[40]Sutton, E. K., "Normalized force coefficients for satellites with elongated shapes," *Journal of Spacecraft and Rockets*, Vol. 46, No. 1, 2009, pp. 112–116.

[41]Sutton, E. K., Nerem, R. S., and Forbes, J. M., "Reply by the authors to G. Koppenwallner," *Journal of Spacecraft and Rockets*, Vol. 45, No. 6, 2008, pp. 1328–1329.

[42]Gregory, J. and Peters, P., "A measurement of the angular distribution of 5 eV atomic oxygen scattered off a solid surface in earth orbit," *Proceedings of the 15th international symposium on rarefied gas dynamics*, edited by V. Boffi and C. Cercignani, Vol. 1, B.G. Teubner, Stuttgart, 1987, pp. 644–656.

[43]Moe, K. and Moe, M. M., "Gas–surface interactions and satellite drag coefficients," *Planetary and Space Science*, Vol. 53, No. 8, 2005, pp. 793–801.

[44]Picone, J., Hedin, A., Drob, D., and Aikin, A., "NRLMSISE-00 empirical model of the atmosphere: Statistical comparisons and scientific issues," *Journal of Geophysical Research*, Vol. 107, No. A12, 2002.

[45]Moe, K., Moe, M., and Rice, C., "Simultaneous analysis of multi-instrument satellite measurements of atmospheric density," *Journal of spacecraft and rockets*, Vol. 41, No. 5, 2004, pp. 849–853.

[46]Sentman, L. H., "Free molecule flow theory and its application to the determination of aerodynamic forces," Tech. Rep. LMSC-448514, Lockheed Missiles  Space Company, 1961.

[47]Moe, K., Moe, M., and Wallace, S., "Improved satellite drag coefficient calculations from orbital measurements of energy accomodation," *Journal of spacecraft and rockets*, Vol. 35, No. 3, 1998, pp. 266–272.

[48]Perosanz, R., "On board evaluation of the STAR accelerometer," *First CHAMP Mission Results for Gravity, Magnetic and Atmospheric Studies*, edited by C. Reigber, H. Lühr, and P. Schwintzer, Springer Verlag, 2003, pp. 11–18.

[49]Doornbos, E., Förster, M., Fritsche, B., van Helleputte, T., van den IJssel, J., Koppenwallner, G., Lühr, H., Rees, D., and Visser, P., "ESTEC contract 21022/07/NL/HE Air density models derived from multi-satellite drag observations – Final Report," Tech. Rep. DEOS / TU Delft scientific report 01/2009, TU Delft, 2009.